# Oxygen permeation and creep behavior of $Ca_{1-x}Sr_xTi_{0.6}Fe_{0.15}Mn_{0.25}O_{3-\delta}$ ($x$=0, 0.5) membrane materials

Jonathan. M. Polfus[a,*], Wen Xing[a], Goran Pećanac[b], Anita Fossdal[a], Sidsel M. Hanetho[a], Yngve Larring[a], Jürgen Malzbender[b], Marie-Laure Fontaine[a], Rune Bredesen[a]

[a]*SINTEF Materials and Chemistry, Forskningsveien 1, NO-0314 Oslo, Norway*

[b]*Forschungszentrum Jülich GmbH, IEK-2, 52425 Jülich, Germany*

[*]Contact email: jonathan.polfus@sintef.no

**Abstract**

Oxygen permeation measurements were performed on dense symmetric samples of $Ca_{0.5}Sr_{0.5}Ti_{0.6}Fe_{0.15}Mn_{0.25}O_{3-\delta}$ and compared to $CaTi_{0.6}Fe_{0.15}Mn_{0.25}O_{3-\delta}$ in order to assess the influence of the perovskite lattice volume on oxygen permeation. Oxygen flux measurements were performed in the temperature range 700-1000 °C and as function of feed side $\boldsymbol{p_{O_2}}$ from $10^{-2}$ to 1 bar, and at high pressures up to 4 bar with a $p_{O_2}$ of 3.36 bar. The $O_2$ permeability of the Sr-doped sample was significantly lower than that of the Sr-free sample, amounting to $3.9\times10^{-3}$ mL min$^{-1}$ cm$^{-1}$ at 900 °C for a feed side $p_{O_2}$ of 0.21 bar. The $O_2$ permeability of $CaTi_{0.6}Fe_{0.15}Mn_{0.25}O_{3-\delta}$ shows little variation with increased feed side pressures and reaches $1.5\times10^{-2}$ mL min$^{-1}$ cm$^{-1}$ at 900 °C for a feed side $p_{O_2}$ of 3.36 bar. This is approximately 1.5 times higher than the $O_2$ permeability with a feed side $p_{O_2}$ of 0.21 bar. Furthermore, in order to assess the applicability of $CaTi_{0.6}Fe_{0.15}Mn_{0.25}O_{3-\delta}$ as an oxygen membrane material, creep tests were performed under compressive loads of 30 and 63 MPa, respectively, in air in the temperature range 700-1000 °C; the results indicate a high creep resistance for this class of materials. The measured $O_2$ permeabilities and creep rates are compared with other state-of-the-art membrane materials and their performance for relevant applications is discussed in terms of chemical and mechanical stability.

**Keywords**: *dense ceramic oxygen membrane; ambipolar transport; creep; $CaTiO_3$; calcium titanate*

## 1. Introduction

Ceramic membranes based on mixed ionic and electronic conductors may be utilized for high temperature oxygen separation from air – enabling, for instance, oxy-fuel combustion or gasification of coal and biomass at higher efficiency compared to cryogenic distillation of oxygen [1,2]. Catalytic membrane reactors may also utilize such membranes for partial oxidation of methane to synthesis gas, oxidative coupling of methane and oxidative dehydrogenation processes [3–9].

The key properties of the membrane material are oxygen flux and stability at operating conditions comprising 1) chemical stability under oxidizing and reducing conditions, $CO_2$ and sulfur containing atmospheres and temperatures above 700 °C (depending on the process conditions); 2) kinetic stability (resistance to kinetic demixing) in oxygen chemical potential gradients; 3) mechanical stability in terms of creep and thermal/chemical expansion [3,4,9–14]. Integration of the membrane in a module also requires chemical compatibility and adequate matching of thermal expansion coefficient with appropriate high temperature alloys. Additionally, cost and toxicity of the materials are important issues for up-scaled production.

It has proven challenging to develop membranes that can meet all of these criteria. The Sr/Ba and Co-containing perovskites exhibit high $O_2$ fluxes [15–18], but suffer from kinetic demixing and poor thermodynamic and mechanical stability [13,16,19–24]. We have recently pursued a stable base material – $CaTi_{0.85}Fe_{0.15}O_{3-\delta}$ (CTF15) – towards improved $O_2$ flux [25–31].

In these materials, oxygen permeation proceeds according to ambipolar transport of oxide ions – by means of oxygen vacancies, $v_O^{\cdot\cdot}$, in Kröger-Vink [32] notation – and electronic charge carriers. Ambipolar conductivity is therefore facilitated by the addition of lower-valent dopants such as $Fe^{3+}$ on the Ti-site, which, according to electroneutrality, will promote the concentrations of oxygen vacancies and electron holes [33]. Increasing the Fe-dopant concentration beyond $x = 0.15$-$0.2$ in $CaTi_{1-x}Fe_xO_{3-\delta}$, however, lowers the $O_2$ flux due to lower oxide ion conductivity associated with trapping of oxygen vacancies and partial transition to an ordered brownmillerite $Ca_2Fe_2O_5$ [26,34–38].

Recently, we have shown that addition of Mn on the Ti-site enhances the $O_2$ permeability with a maximum flux obtained for $CaTi_{0.6}Fe_{0.15}Mn_{0.25}O_{3-\delta}$; the improvement was associated mainly with increased electronic conductivity [27,28]. The activation energy of the $O_2$ permeability was found to increase close to linearly with Mn-content. This was ascribed to an increased activation energy of oxide ion transport due to a linear lowering of the lattice volume with Mn-content. In light of these findings, we have investigated the effect of substituting Sr on the Ca-site of $CaTi_{0.6}Fe_{0.15}Mn_{0.25}O_{3-\delta}$ as a means to increase the lattice volume and potentially lower the activation energy of oxide ion transport, while presumably attaining a cubic symmetry compared to introducing a larger cation on the Ti-site.

In this work, we present structure data and $O_2$ permeation measurements of densely sintered disc samples of $Ca_{0.5}Sr_{0.5}Ti_{0.6}Fe_{0.15}Mn_{0.25}O_{3-\delta}$ (CSTFMn25) in comparison with the respective Sr-free composition. The effect of pressures of up to 4 bar and $\boldsymbol{p_{O_2}}$ of 3.36 bar is evaluated with respect to the $O_2$ permeability of $CaTi_{0.6}Fe_{0.15}Mn_{0.25}O_{3-\delta}$ (CTFMn25). While Sr-containing compounds tend to exhibit limited stability towards $CO_2$, this may not be the case for the addition of Sr to the $CaTiO_3$ based material; the higher stability of the cubic $SrTiO_3$ structure compared to $CaTiO_3$ more than compensates for the higher stability of $SrCO_3$ relative to $CaCO_3$ [39]. Furthermore, creep measurements were performed on compressively loaded CTFMn25 specimens in order to determine mechanical stability under operating conditions. The creep behavior of an Mn-free composition, $CaTi_{0.9}Fe_{0.1}O_{3-\delta}$ (CTF10), was also measured for comparison. Finally, the results from $O_2$ flux and creep rate measurements are reviewed in relation to state-of-the-art membrane materials.

## 2. Experimental

### 2.1 Sample preparation and characterization

$Ca_{0.5}Sr_{0.5}Ti_{0.6}Fe_{0.15}Mn_{0.25}O_{3-\delta}$ (CSTFMn25) was synthesized according to a Pechini-type route using nitrate salts as starting agents, citric acid as a complexing agent and ethylene glycol for polymerization. Sols were pre-calcined at 400 °C, and the resulting powders were manually crushed in an agate mortar, and further annealed at 900 °C for 6 h in ambient air. Details of the synthesis procedure, which was also used for preparation of the CTFMn25, are described in Ref. [27]. Uniaxially pressed disc samples (∅ = 20 mm) were sintered at 1300 °C for 6 h in ambient air. The sintered disc samples were gradually polished to a roughness of 6 μm and 1 μm with SiC grinding paper and diamond paste, respectively. The final thicknesses of the membranes for flux measurements were 1.23 and 1.50 mm for CSTFMn25 and CTFMn25, respectively.

For creep measurements, uniaxial pressed cylindrical specimens of CTFMn25 (∅ = 7 mm) were sintered according to the same procedure. The final dimensions were 12 mm length

and 5.4 mm diameter. Additionally, porous tubular CTF10 specimens were prepared by plastic extrusion including pyrolyzable pore formers as described in Ref. [40] The tubular specimens were sintered at 1380 °C for 5 h in air, and the final dimensions were 30 mm length, 9.3 mm outer diameter and 1.1 mm wall thickness.

For X-ray diffraction (XRD), sintered samples were crushed and analyzed using a Bruker D8 Focus diffractometer with Cu Kα radiation and LynxEye detector. The diffraction data were analyzed using the Rietveld method as implemented in the TOPAS software by Bruker. Porosity and grain size were graphically analyzed from optical micrographs using the AnalySIS software, where the grain size was taken as the equivalent circular diameter (ECD) value.

### 2.2 $O_2$ flux measurements

The sintered disc samples were sealed to alumina support tubes (∅ = 12 mm) in a ProboStat measurement cell (NorECs, Norway) with gold O-ring gaskets. Each sample was pressed against the gold gasket and alumina support tube with a force of approx. 45 N with an alumina spring load assembly during sealing and measurements. Mass flow controllers were utilized to supply $O_2$/He feed gas mixtures and Ar sweep gas at 50 and 25 mL $min^{-1}$, respectively, and back-pressure controllers on the feed and sweep side outlets enabled pressures above ambient. The concentrations of $O_2$ permeate and He leakage were measured with a Varian CP-4900 gas chromatograph (GC). The measurements cell was mounted in a vertical tube furnace and temperature was monitored with an S-type thermocouple placed in the vicinity of the sample and gold O-ring inside the measurement cell. Gas tight seals were obtained by heating to 1000 °C in air, and the He leakage rate for all measurements was well below 1 % of the $O_2$ permeation. Ambient pressure $O_2$ fluxes were measured at temperatures between 700-1000 °C and as function of feed side oxygen partial pressure, $\boldsymbol{p_{O_2}}$, in the range from $10^{-2}$ to 1 bar. $O_2$ fluxes under high-pressure were measured in ambient feed side mixtures of 0.21, 0.42 and 0.84 bar $O_2$ pressurized to 2 and 4 bars, corresponding to $\boldsymbol{p_{O_2}}$ of 0.42-3.36 bar. For these measurements, the sweep side Ar was pressurized to 100 mbar below the feed side pressure in order to avoid mechanical failure of the membrane or gold O-ring gasket. The $O_2$ flux through a dense ceramic membrane, $j_{O_2}$, can be expressed from ambipolar conductivity, $\sigma_{amb}$, according to

$$j_{O_2} = \frac{RT}{16F^2L}\int_{p^s_{O_2}}^{p^f_{O_2}} \sigma_{amb}\, d\ln p_{O_2} \quad (1)$$

where $p^f_{O_2}$ and $p^s_{O_2}$ refer to the feed and sweep side, respectively, $L$ is the thickness of the membrane and F is the Faraday constant. The $O_2$ permeability, $J_{O_2}$, is taken as the thickness normalized $O_2$ flux with units mL(STP) $min^{-1}$ $cm^{-1}$ at specified feed and sweep side conditions.

### 2.3 Creep measurements

The creep behavior of CTFMn25 and CTF10 was assessed with compression tests carried out on an Instron 1362 machine in the temperature range from 850 °C to 1000 °C in an ambient air. Dense cylindrical CTFMn25 specimens as well as porous tubular CTF10 specimens were uniaxially loaded between the two base plates. In order to minimize surface effects and superimposed bending induced by misalignments, the flatness and the parallelism of these previously ground and polished base surfaces was ensured to be 0.04 mm and 0.1 mm, respectively. The deformation of the specimens was indirectly measured by three equidistant sensors at a radial angle of 60°, which measured the relative movement of the loading and supporting base plate. The sensors were attached to a ceramic extension rod connected to a linear variable differential transformer (Sangamo, LVDT, range ± 1 mm, precision 1.25 μm). The load was measured by a load cell of 10 kN range (1210 ACK, Interface Company). The

temperature was controlled by a K-type thermocouple placed in close vicinity of the specimen. The specimens were heated at 8 °C $min^{-1}$ with a pre-load of 2 N. The applied stresses were 30 MPa and 63 MPa, which is a realistic stress range in a membrane application according to Schulz et al. [41] The loads were applied stepwise at constant temperature. Heating sequences were applied in the considered temperature range with steps of 50 °C. At each temperature, the sample was allowed to equilibrate for a minimum of 1 h before the actual compressive creep load was applied. In all cases the creep load was applied for at least 24 hours to assure that a secondary creep stage is reached.

The compressive strain rate was calculated as the ratio of the measured linear deformation over time and the initial height. An Arrhenius approach [42] was used to describe the creep rate according to

$$\dot{\varepsilon} = A\,\sigma^{n}\exp\left(-\frac{E_a}{R\,T}\right) \quad (1)$$

where $A$ is a constant, $n$ is the stress exponent, $\sigma$ is the applied stress, $E_a$ is the activation energy, $R$ is the universal gas constant and $T$ the temperature. The stress exponent $n$ was determined from a $\ln\dot{\varepsilon}$–$\ln\sigma$ plot, whereas the activation energy $E_a$ was obtained from a $\ln\dot{\varepsilon}$–$1000/T$ plot.

## 3. Results and discussion

### 3.1 X-ray diffraction

Figure 1 shows powder X-ray diffractograms of the sintered CSTFMn25 and CTFMn25 samples – both samples exhibit single-phase perovskite structure and no apparent secondary phases. The CSTFMn25 pattern was refined with the P$m\bar{3}m$ space group with $a$ = 3.84 Å, and CTFMn25 pattern was refined with the P$bnm$ space-group and $a$ = 5.37 Å, $b$ = 5.39 Å, and $c$ = 7.60 Å. The apparent satellite peaks at lower angle (most evident at approx. 31° for CSTFMn25) can be attributed to tube tails due to the rather high acquisition time and low background. The lattice volume of CSTFMn25, 56.62 $Å^3$, is approx. 3.4 % larger than the pseudocubic lattice volume of CTFMn25, and corresponds well with an expected increase of approx. 3.7 % by considering the ionic radii of 12-coordinated $Ca^{2+}$ and $Sr^{2+}$ [43].

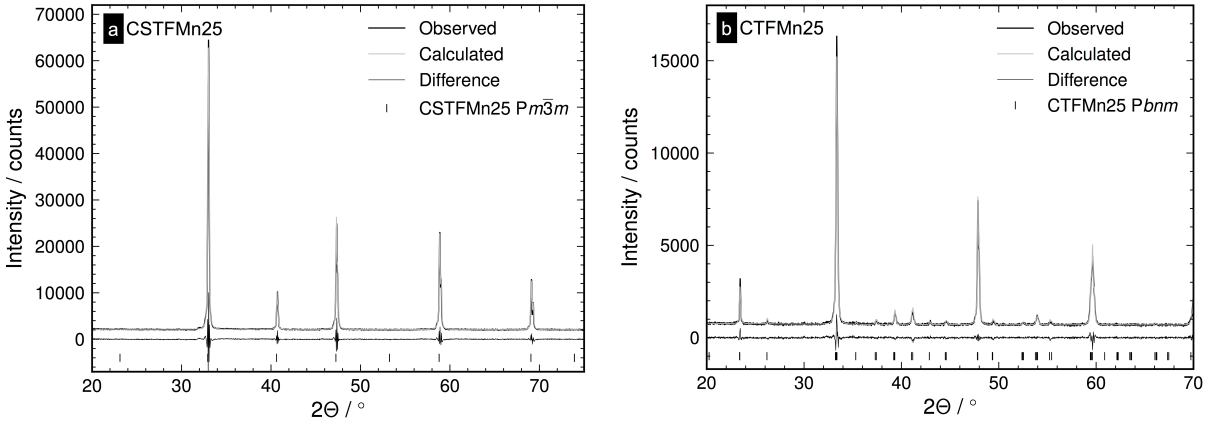


Figure 1: Powder X-ray diffractograms of the sintered samples of CSTFMn25 (a) and CTFMn25 (b).

### 3.2 $O_2$ permeability

The $O_2$ permeabilities of CSTFMn25 and CTFMn25 are compared as function of inverse temperature in Figure 2a for a feed side $p_{O_2}$= 0.21 bar. The $O_2$ permeability of CSTFMn25 is lower than CTFMn25 at all temperatures, and furthermore, exhibits a discontinuity below 800 °C. A similar discontinuity in $J_{O_2}$ was observed for $CaTi_{0.85}Fe_{0.15}O_{3-\delta}$ (CTF15) at the same

temperature [27]. Reduction in oxide ion conductivity of more than one order of magnitude has been reported below 1000 °C for higher Fe-dopant concentrations, $CaTi_{0.8}Fe_{0.2}O_{3-\delta}$ [44,45]. This reduction in oxide ion conductivity was associated with ordering of oxygen vacancies, and accordingly, it seems that the CTF15 and CSTFMn25 samples exhibit partial ordering of oxygen vacancies at slightly lower temperature, i.e., 775-800 °C.

Figure 2b shows an Arrhenius type plot of $J_{O_2} \cdot T$ with linear fits and corresponding activation energies in two main temperature regimes: 1000-900 and 900-700 °C. CSTFMn25 exhibits a considerable increase in activation energy compared to CTFMn25 in both regimes. With respect to lattice volume, this trend is opposite of that found for the $CaTi_{0.85-x}Fe_{0.15}Mn_xO_{3-\delta}$ ($x$ = 0-0.4) system where the activation energy of $J_{O_2}$ was found to increase close to linearly with Mn-content and reduced lattice volume [28].

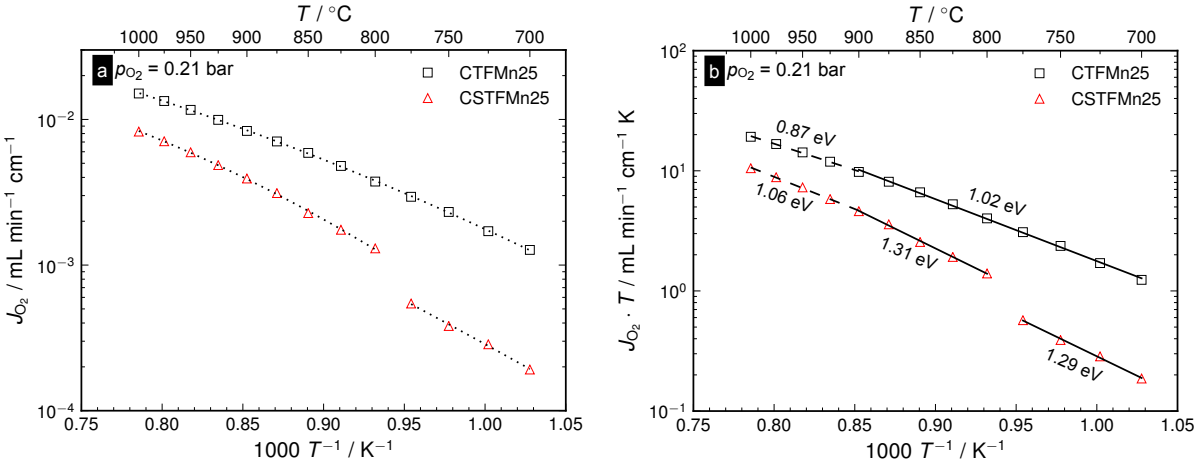


Figure 2: $O_2$ permeability as function of inverse temperature (a) and Arrhenius type plot with linear fits and corresponding activation energies (b) for feed side $p_{O_2}$=0.21 bar.

Figure 3 shows the $O_2$ permeability as function of feed side $p_{O_2}$ at 700-1000 °C for CSTFMn25 and CTFMn25. The functional dependencies of $J_{O_2}$ with feed side $p_{O_2}$ are quite similar for both samples with a transition from approx. $\frac{1}{4}$ at low $p_{O_2}$ and lower temperatures to a slightly lower functional dependency at higher $p_{O_2}$ and temperatures. A functional dependency of approximately $J_{O_2} \propto p_{O_2}^{\frac{1}{4}}$ corresponds to limiting p-type electronic conductivity while a lower functional dependency indicates a lower p-type influence and $J_{O_2}$ approaching to be proportional to the driving force, i.e., $\log\left(\frac{p_{O_2}^{f}}{p_{O_2}^{s}}\right)$, under our measurement conditions [27]. CSTFMn25 exhibits slightly lower functional dependencies of $J_{O_2}$ with feed side $p_{O_2}$, and accordingly it seems that $J_{O_2}$ is less limited by electronic conductivity than in the case of CTFMn25, particularly at high temperature and high feed side $p_{O_2}$. This can be explained by a similar electronic conductivity of CSTFMn25 and CTFMn25, given the same Mn-content, and a lower oxide ion conductivity of CSTFMn25. The $O_2$ permeability of CSTFMn25 at 900 °C and feed side $p_{O_2}$ = 0.21 bar, $3.9\times10^{-3}$ mL min$^{-1}$ cm$^{-1}$, is lower than that reported for the similarly B-site doped $Sr_{0.97}Ti_{0.6}Fe_{0.4}O_{3-\delta}$, $7.2\times10^{-3}$ mL min$^{-1}$ cm$^{-1}$ [46].

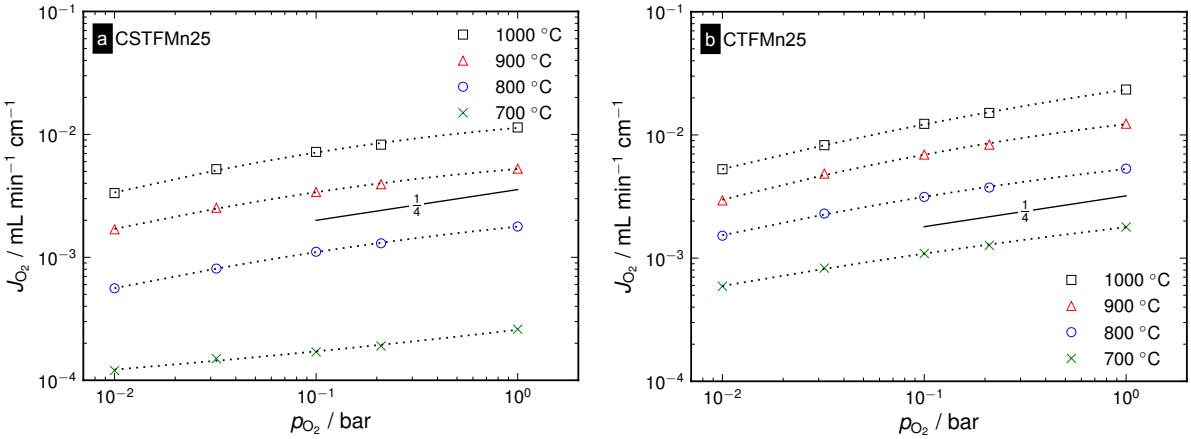


Figure 3: $O_2$ permeability as function of feed side $p_{O_2}$ at temperatures from 700-1000 °C for CSTFMn25 (a) and CTFMn25 (b).

Figure 4a shows the $O_2$ permeability of CTFMn25 as function of $p_{O_2}$ up to 3.36 bar and total pressure up to 4 bar. The functional dependency of $J_{O_2}$ with respect to feed side $p_{O_2}$ is slightly less than $\frac{1}{4}$ and becomes gradually lower at higher $p_{O_2}$. This may be explained by constant oxide ion conductivity determined by the dopant concentration and a significantly higher p-type electronic conductivity. Under this condition the driving force normalized $O_2$ permeability, i.e., $J_{O_2}/\log\left(\frac{p^f_{O_2}}{p^s_{O_2}}\right)$, is representative of the ambipolar conductivity (see Eq. 1). In Figure 4b, the driving force normalized $O_2$ permeability is found to be fairly constant at each isotherm as expected. The small increase in value at constant temperature with increasing feed side oxygen partial pressure indicates that a slight influence of electronic conductivity on the permeability still exists.

It should be noted that that in Figure 4a, increased feed side oxygen pressure does not significantly enhance the $O_2$ permeability of CTFMn25. This is merely due to the small increase in driving force under constant sweep flow condition since $p^s_{O_2}$ increases with $J_{O_2}$ during our measurements. The $O_2$ permeability of CTFMn25 reaches $1.5\times10^{-2}$ mL min$^{-1}$ cm$^{-1}$ at 900 °C for a feed side $p_{O_2}$= 3.36 bar, which is approx. 1.5 times higher than that with $p_{O_2}$= 0.21 bar, $9.4\times10^{-3}$ mL min$^{-1}$ cm$^{-1}$.

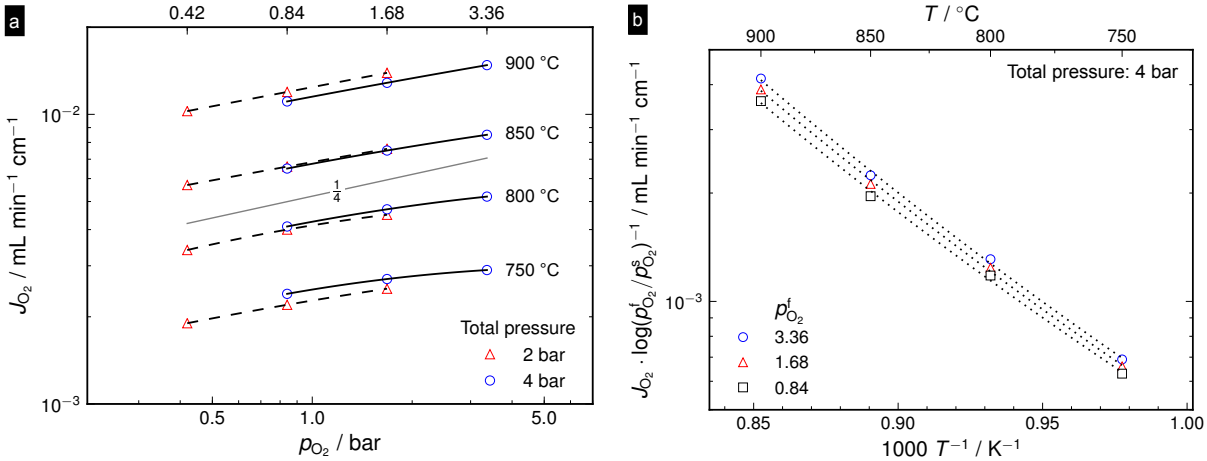


Figure 4: $O_2$ permeability of CTFMn25 as function of feed side $p_{O_2}$ from 0.21-3.36 bar for total pressures of 2 and 4 bar and temperatures between 750-900 °C (a), and driving force normalized $O_2$ permeability at 4 bar total pressure as function of inverse temperature (b). The measurements were conducted from high to low temperature.

### 3.3 Creep behavior

Figure 5 shows the creep rate of CTFMn25 as function of inverse temperature for compressive loads of 30 and 63 MPa, as well as literature data on other relevant membrane materials. CTFMn25 exhibits high creep resistance, confirming the potential of this material for high temperature applications. In comparison, $La_{0.38}Sr_{0.6}Co_{0.2}Fe_{0.8}O_{3-\delta}$ (LSCF) [11], $La_{0.58}Sr_{0.4}Co_{0.2}Fe_{0.8}O_{3-\delta}$ (LSCF58) [22] and $Ba_{0.5}Sr_{0.5}(Co_{0.8}Fe_{0.2})_{0.97}Zr_{0.03}O_{3-\delta}$ (BSCFZ) [24] exhibit higher creep rates with similar activation energies. Creep rates for BSCFZ are almost identical to the ones of the frequently studied BSCF membrane material [23]. On the other hand, $Ce_{0.8}Gd_{0.2}O_{2-\delta}$ (CG) [11] exhibits a considerably lower creep rate at 900 °C for a stress of 63 MPa (Figure 5b).

From the optical surface micrographs of the CTFMn25 and CTF10 specimens in Figure 6, porosities of below 1 % and 30 % were obtained for CTFMn25 and CTF10 with average grain sizes of 5 ± 2 µm and 2 ± 1 µm, respectively. Evaluation of the creep data on CTFMn25 revealed a stress exponent of 1.5, implying that creep was dominated by a diffusional mechanism. The determined activation energy of 5.1 ± 0.4 eV excluded oxide ions as the rate controlling species [16] and implied that cation diffusion is rate controlling for creep in these materials. The creep data on CTF10 exhibited a stress exponent of 1.6 and activation energy of 4.4 ± 1.1 eV which implies a similar creep mechanism as for CTFMn25. However, porosity and grain size also have to be taken into account when comparing the creep rate of different specimens: creep deformation increases with porosity and decreases with larger grain size, especially for a diffusional creep mechanism. Considering the significant porosity of the CTF10 specimen and rather similar grain sizes, the lower creep rate of CTF10 indicates a decrease in creep resistance with Mn-doping for CTFMn25.

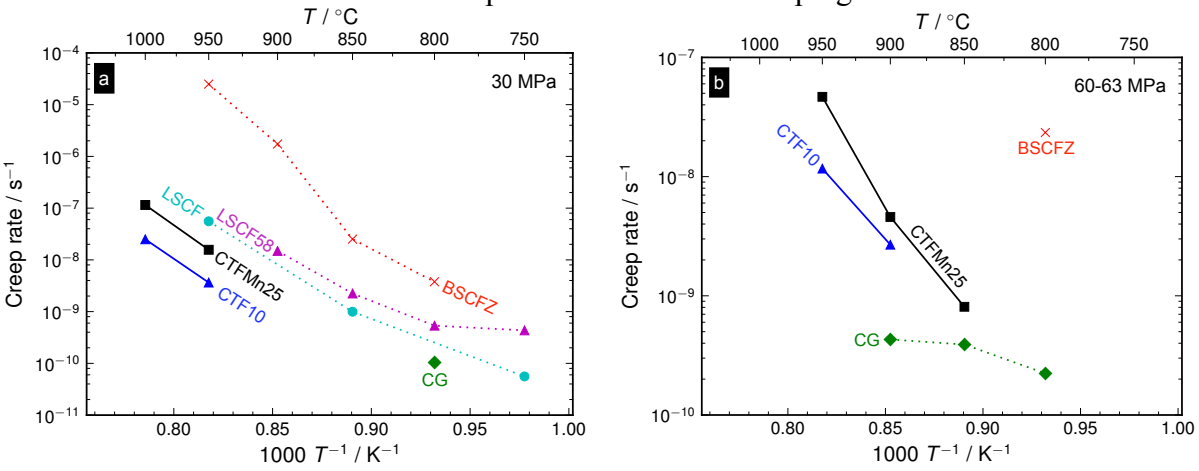


Figure 5: Measured creep rate of dense CTFMn25 and porous CTF10 under a compressive load of 30 MPa (a) and 63 MPa (b). For comparison, literature data are added for dense $La_{0.38}Sr_{0.6}Co_{0.2}Fe_{0.8}O_{3-\delta}$ (LSCF, 30 MPa load)[11], $La_{0.58}Sr_{0.4}Co_{0.2}Fe_{0.8}O_{3-\delta}$ (LSCF58, 30 MPa load) [22], $Ce_{0.8}Gd_{0.2}O_{2-\delta}$ (CG, 30 and 60 MPa load) [11], and $Ba_{0.5}Sr_{0.5}(Co_{0.8}Fe_{0.2})_{0.97}Zr_{0.03}O_{3-\delta}$ (BSCFZ, 30 and 63 MPa load) [24].

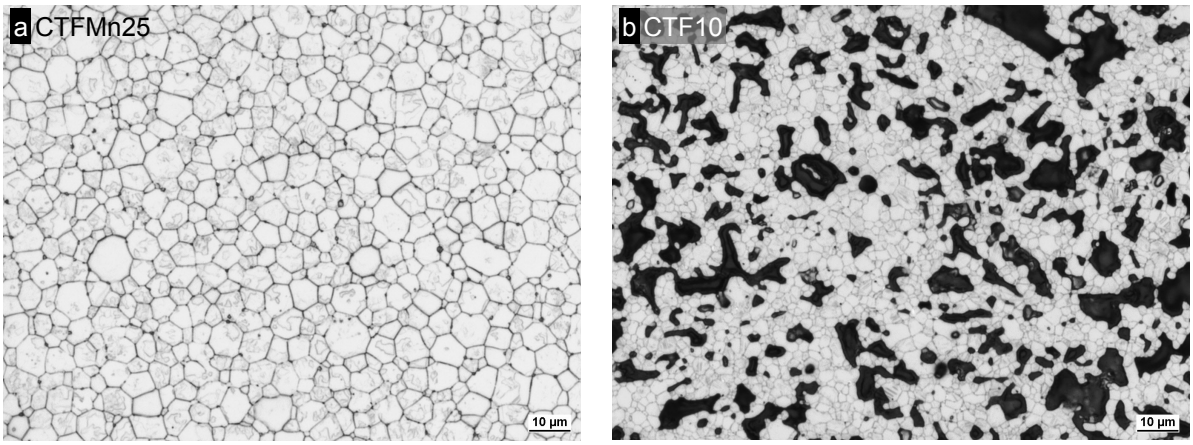

Figure 6: Optical surface micrograph of the specimens used in creep tests of CTFMn25 (a) and CTF10 (b).

### 3.4 Evaluation of material applicability

The $O_2$ permeability of CTFMn25 is compared to a range of other oxygen membrane materials from literature in Figure 7; the performance of CTFMn25 lags approx. 30-50 times behind the state-of-the-art membranes. In order to achieve a target $O_2$ flux of 10 mL min$^{-1}$ cm$^{-2}$ at 900 °C [47], the membrane thickness would need to be approx. 8 µm for CTFMn25 and in the 100-300 µm range for BSF, BSCF, CG-MF and BCCF (see Figure 7). However, the chemical and mechanical stability of the membrane under operating conditions – crucial for practical application – must be considered. The Ba/Sr containing materials generally suffer from low chemical stability towards $CO_2$ and $SO_2$ due to formation of carbonates and sulfates, rendering these materials unfit for long term operation in contact with these gases.[48–51] Sufficient stability towards $CO_2$ may, however, be achieved for lower $CO_2$ concentrations, e.g., 5% $CO_2$ at 875 °C during 400 h of partial oxidation of methane with a $Ba_{0.9}Co_{0.7}Fe_{0.2}Nb_{0.1}O_{3-\delta}$ membrane [52]. The long-term stability of asymmetric tubular membranes based on CTFMn25 has been demonstrated for more than 6 months operation at 900 °C mainly in CO/$CO_2$ containing atmospheres [29]. Other novel $O_2$ membrane materials that are stable towards $CO_2$ and/or $SO_2$ include $SrFe_{0.8}Nb_{0.2}O_{3-\delta}$ [53], $La_{0.6}Ca_{0.4}FeO_{3-\delta}$ [54], and $NiFe_2O_4$−$Ce_{0.8}Tb_{0.2}O_{2-\delta}$ composites [55], with $O_2$ permeabilities of 0.025, 0.016 and 0.007 mL min$^{-1}$ cm$^{-1}$, respectively, at 900 °C for a feed side $p_{O_2}$ = 0.21 bar; these values are in the same range as CTFMn25. Membranes based on $La_{0.8}Sr_{0.2}GaO_{3-\delta}$ and composites in the $CeO_2$-$MnFe_2O_4$ system exhibit significantly higher $O_2$ permeabilities and show great promise for partial oxidation of methane [56–59]. Furthermore, CTFMn25 is promising with respect to low cost and non-toxicity, while in this respect elements such as Ga, Tb and Co are much more challenging for up-scaled membrane production. Finally, with respect to mechanical stability, $CaTiO_3$ and CTFMn25 exhibit high creep resistance [60,61]. $LaGaO_{3-\delta}$ and $CeO_{2-\delta}$ based membranes also exhibit high creep resistance, while some compositions of the latter are prone to significant chemical expansion at high temperatures [11,12,62]. $LaFeO_{3-\delta}$ based materials can be expected to also exhibit sufficient creep resistance due to rather low cation diffusivities [63,64]. The creep resistance of the $CeO_{2-\delta}$ based composites is however uncertain and should be investigated for further evaluation of these materials as oxygen membranes. The Ba/Sr and Co containing membranes generally exhibit low creep resistance [23,42,65], and Zr-doping has not been found to notably improve the creep resistance of these materials [14,66].

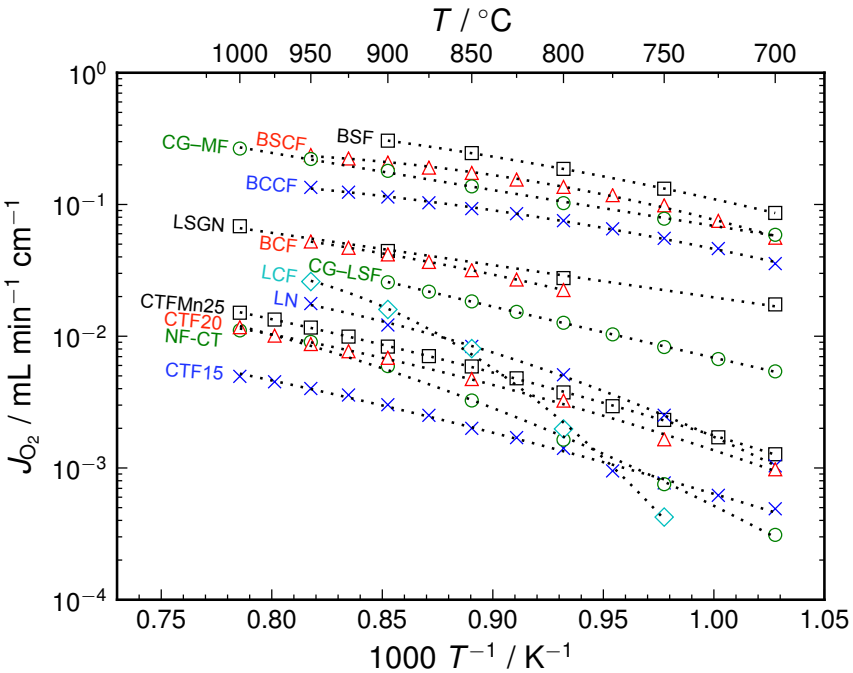


Figure 7: $O_2$ permeability of CTFMn25 (present work) as function of inverse temperature compared literature data on $Ba_{0.3}Sr_{0.7}FeO_{3-\delta}$ (BSF) [67], $Ba_{0.5}Sr_{0.5}Co_{0.8}Fe_{0.2}O_{3-\delta}$ (BSCF) [16], $Ce_{0.8}Gd_{0.2}O_{2-\delta}$ containing 15 vol% $MnFe_2O_4$ (CG-MF) [56], $BaCe_{0.1}Co_{0.4}Fe_{0.5}O_{3-\delta}$ (BCCF) [68], $La_{0.8}Sr_{0.2}Ga_{0.7}Ni_{0.3}O_{3-\delta}$ (LSGN) [58], $BaCe_{0.15}Fe_{0.85}O_{3-\delta}$ (BCF) [69], $Ce_{0.9}Gd_{0.1}O_{2-\delta}$ containing $La_{0.6}Sr_{0.4}FeO_{3-\delta}$ (CG-LSF) [70], $La_{0.6}Ca_{0.4}FeO_{3-\delta}$ (LCF) [54], $La_2NiO_{4+\delta}$ (LN) [71], $CaTi_{0.8}Fe_{0.2}O_{3-\delta}$ (CTF20) [26], $NiFe_2O_4$ containing 40 vol% $Ce_{0.8}Tb_{0.2}O_{2-\delta}$ (NF-CT) [55] and $CaTi_{0.85}Fe_{0.15}O_{3-\delta}$ (CTF15) [27]. All data are for feed side $p_{O_2}$=0.21 bar and for samples with thicknesses in the mm-range, and in some cases with catalytic layers applied to the sample surfaces. Still, it should be noted that the reported fluxes may be influenced by surface kinetics.

## 4. Conclusions

The $O_2$ permeability CSTFMn25 is lower than that of CTFMn25 at temperatures between 1000-700 °C for a feed side $p_{O_2}$ in the range $10^{-2}$ to 1 bar, and CSTFMn25 exhibits a considerably larger activation energy of $J_{O_2}$. For CTFMn25, a moderate improvement of $J_{O_2}$ is found for increased feed side pressures up to 4 bar, reaching $1.5\times10^{-2}$ mL $min^{-1}$ $cm^{-1}$ at 900 °C for a feed side $p_{O_2}$= 3.36 bar. Creep measurements on CTFMn25 indicate a diffusional creep mechanism and high creep resistance compared to other membrane materials. Despite the rather low $O_2$ flux, CTFMn25 based membranes may be a viable candidate when considering chemical and mechanical stability, cost and toxicity.

## 5. Acknowledgements

This research has received funding from the European Union Seventh Framework Programme (FP7/2007-2013) via grant agreement no. FP7-ENERGY-268165, “Highly Efficient Tubular Membranes for Oxy-Combustion” (HETMOC). The authors are grateful to Ms. Tatjana Osipova (Forschungszentrum Jülich) for experimental support.

## 6. References

[1] IEA, Technology Roadmap: Carbon capture and storage, 2013.

[2] S.S. Hashim, a. R. Mohamed, S. Bhatia, Oxygen separation from air using ceramic-based membrane technology for sustainable fuel production and power generation, Renew. Sustain. Energy Rev. 15 (2011) 1284–1293.

[3] P.V. Hendriksen, P.H. Larsen, M. Mogensen, F.W. Poulsen, K. Wiik, Prospects and problems of dense oxygen permeable membranes, Catal. Today. 56 (2000) 283–295.

[4] H.J.M. Bouwmeester, Dense ceramic membranes for methane conversion, Catal. Today. 82 (2003) 141–150.

[5] A. Thursfield, I.S. Metcalfe, The use of dense mixed ionic and electronic conducting membranes for chemical production, J. Mater. Chem. 14 (2004) 2475.

[6] M. Rebeilleau-Dassonneville, S. Rosini, A.C. van Veen, D. Farrusseng, C. Mirodatos, Oxidative activation of ethane on catalytic modified dense ionic oxygen conducting membranes, Catal. Today. 104 (2005) 131–137.

[7] W. Yang, H. Wang, X. Zhu, L. Lin, Development and Application of Oxygen Permeable Membrane in Selective Oxidation of Light Alkanes, Top. Catal. 35 (2005) 155–167.

[8] J. Sunarso, S. Baumann, J.M. Serra, W.A. Meulenberg, S. Liu, Y.S. Lin, et al., Mixed ionic–electronic conducting (MIEC) ceramic-based membranes for oxygen separation, J. Memb. Sci. 320 (2008) 13–41.

[9] K. Zhang, J. Sunarso, Z. Shao, W. Zhou, C. Sun, S. Wang, et al., Research progress and materials selection guidelines on mixed conducting perovskite-type ceramic membranes for oxygen production, RSC Adv. 1 (2011) 1661.

[10] P.-M. Geffroy, J. Fouletier, N. Richet, T. Chartier, Rational selection of MIEC materials in energy production processes, Chem. Eng. Sci. 87 (2013) 408–433.

[11] M. Lipińska-Chwałek, G. Pećanac, J. Malzbender, Creep behaviour of membrane and substrate materials for oxygen separation units, J. Eur. Ceram. Soc. 33 (2013) 1841–1848.

[12] G. Pećanac, S. Foghmoes, M. Lipińska-Chwałek, S. Baumann, T. Beck, J. Malzbender, Strength degradation and failure limits of dense and porous ceramic membrane materials, J. Eur. Ceram. Soc. 33 (2013) 2689–2698.

[13] G. Pećanac, S. Baumann, J. Malzbender, Mechanical properties and lifetime predictions for Ba 0.5 Sr 0.5 Co 0.8 Fe 0.2 O 3− δ membrane material, J. Memb. Sci. (2011).

[14] V. Stournari, S.F.P. ten Donkelaar, J. Malzbender, L. Singheiser, H.J.M. Bouwmeester, Creep behavior of perovskite-type oxides Ba0.5Sr0.5(Co0.8Fe0.2)1−xZrxO3−δ, J. Eur. Ceram. Soc. 35 (2015) 1841–1846.

[15] Y. Teraoka, H.-M. Zhuang, S. Furukawa, N. Yamazoe, Oxygen permeation through Perovskite-type oxides, Chem. Lett. (n.d.) 1743–1746.

[16] Z. Shao, W. Yang, Y. Cong, H. Dong, J. Tong, G. Xiong, Investigation of the permeation behavior and stability of a Ba0.5Sr0.5Co0.8Fe0.2O3 oxygen membrane, J. Memb. Sci. 172 (2000) 177–188.

[17] J. Tong, W. Yang, R. Cai, B. Zhu, G. Xiong, L. Lin, Investigation on the structure stability and oxygen permeability of titanium-doped perovskite-type oxides of BaTi0.2CoxFe0.8−xO3−δ (x=0.2–0.6), Sep. Purif. Technol. 32 (2003) 289–299.

[18] S. Baumann, J.M. Serra, M.P. Lobera, S. Escolástico, F. Schulze-Küppers, W. a. Meulenberg, Ultrahigh oxygen permeation flux through supported Ba0.5Sr0.5Co0.8Fe0.2O3−δ membranes, J. Memb. Sci. 377 (2011) 198–205.

[19] L. Qiu, T.H. Lee, L.-M. Liu, Y.L. Yang, A.J. Jacobsen, Oxygen permeation studies of SrCo0.8Fe0.2O3 − δ, Solid State Ionics. 76 (1995) 321–329.

[20] A. Thursfield, I.S. Metcalfe, Air separation using a catalytically modified mixed conducting ceramic hollow fibre membrane module, J. Memb. Sci. 288 (2007) 175–187.

[21] H. Lein, K. Wiik, T. Grande, Kinetic demixing and decomposition of oxygen permeable membranes, Solid State Ionics. 177 (2006) 1587–1590.

[22] B.X. Huang, R.W. Steinbrech, S. Baumann, J. Malzbender, Creep behavior and its correlation with defect chemistry of La0.58Sr0.4Co0.2Fe0.8O3−δ, Acta Mater. 60 (2012) 2479–2484.

[23] B. Rutkowski, J. Malzbender, R.W. Steinbrech, T. Beck, H.J.M. Bouwmeester, Influence of thermal history on the cubic-to-hexagonal phase transformation and creep behaviour of Ba0.5Sr0.5Co0.8Fe0.2O3-δ ceramics, J. Memb. Sci. 381 (2011) 221–225.

[24] G. Pećanac, L. Kiesel, J. Malzbender, Steady-state creep of porous and an extended analysis on the creep of dense BSCFZ perovskite, J. Memb. Sci. 456 (2014) 134–138.

[25] T. Esaka, T. Fujii, K. Suwa, H. Iwahara, Electrical conduction in CaTi1−xFexO3−δ under low oxygen pressure and its application for hydrogen production, Solid State Ionics. 40-41 (1990) 544–547.

[26] F. Figueiredo, M. Soares, Properties of CaTixFexO3 ceramic membranes, J. Electroceramics. (2004) 627–636.

[27] J.M. Polfus, W. Xing, S.M. Hanetho, M.F. Sunding, P.I. Dahl, Y. Larring, et al., Doping strategies for increased oxygen permeability of CaTiO3 based membranes, J. Memb. Sci. (2015).

[28] J.M. Polfus, W. Xing, M. Riktor, P.I. Dahl, M.F. Sunding, S.M. Hanetho, et al., Enhanced O2 Flux of CaTiO3-based membranes by Mn-doping, J. Memb. Sci. (2015).

[29] W. Xing, M.-L. Fontaine, Y. Larring, J.M. Polfus, Z. Li, P. Henriksen, et al., High temperature CaTi0.6Fe0.15Mn0.25O3-δ asymmetric tubular membrane fabrication and oxygen flux characterization, To Be Submitt. (2015).

[30] M. Jacobs, M.-L. Fontaine, R. Bredesen, B. Michielsen, V. Middelkoop, Y. Larring, et al., Surface activation of asymmetric CaTi1−xFexO3−δ tubular membranes for oxygen separation, J. Memb. Sci. 477 (2015) 58–64.

[31] G.C. Mather, M.S. Islam, F.M. Figueiredo, Atomistic Study of a CaTiO3-Based Mixed Conductor: Defects, Nanoscale Clusters, and Oxide-Ion Migration, Adv. Funct. Mater. 17 (2007) 905–912.

[32] F.A. Kröger, H.J. Vink, Relations between the Concentrations of Imperfections in Crystalline Solids, Solid State Phys. - Adv. Res. Appl. 3 (1956) 307–435.

[33] H. Iwahara, T. Esaka, T. Mangahara, Mixed conduction and oxygen permeation in the substituted oxides for CaTiO3, J. Appl. Electrochem. 18 (1988) 173–177.

[34] E. Chinarro, Bulk and grain boundary conductivity of Ca0.97Ti1−xFexO3−δ materials, Solid State Ionics. 160 (2003) 161–168.

[35] A.I. Becerro, C. McCammon, F. Langenhorst, F. Seifert, R. Angel, Oxygen vacancy ordering in CaTiO 3 –CaFeO 2.5 perovskites: From isolated defects to infinite sheets, Phase Transitions. 69 (1999) 133–146.

[36] A. Becerro, F. Seifert, R. Angel, Displacive phase transitions and spontaneous strains in oxygen deficient CaFexTi1-xO3-x/2 perovskites (0<x<0. 40), J. Phys. Condens. Matter. 12 (2000) 3661–3670.

[37] C. McCammon, A.I. Becerro, F. Langenhorst, R.J. Angel, S. Marion, F. Seifert, Short-range ordering of oxygen vacancies in CaFexTi1−xO3−x/2 perovskites (0 <x< 0.4) C, J. Phys. Condens. Matter. 12 (2000) 2969–2984.

[38] F.M. Figueiredo, J. Waerenborgh, V. V Kharton, H. Na, J.R. Frade, On the relationships between structure , oxygen stoichiometry and ionic conductivity of CaTi1-xFexO3, Solid State Ionics. 156 (2003) 371–381.

[39] C.W. Bale, P. Chartrand, S.A. Degterov, G. Eriksson, K. Hack, R. Ben Mahfoud, et al., FactSage thermochemical software and databases, Calphad Comput. Coupling Phase Diagrams Thermochem. 26 (2002) 189–228.

[40] G. Pećanac, J. Malzbender, F. Pauly, M.L. Fontaine, P. Niehoff, S. Baumann, et al., Mechanical characterization of ceramics by means of a 3D defect analysis, Ceram. Int. 41 (2015) 2411–2417.

[41] M. Schulz, R. Kriegel, W. Burckhardt, Modeling of oxygen flux and stress distribution for Ba 0.5 Sr 0.5 Co 0.8 Fe 0.2 O 3-δ membranes at application conditions, Proc. 10th Int. Conf. Inorg. Membr. Tokyo, Japan. (2008).

[42] J.X. Yi, H.L. Lein, T. Grande, S. Yakovlev, H.J.M. Bouwmeester, High-temperature compressive creep behaviour of the perovskite-type oxide Ba0.5Sr0.5Co0.8Fe0.2O3 - δ, Solid State Ionics. 180 (2009) 1564–1568.

[43] R.D. Shannon, Revised effective ionic radii and systematic studies of interatomic distances in halides and chalcogenides, Acta Crystallogr. Sect. A. 32 (1976) 751–767.

[44] S. Marion, A.I. Becerro, T. Norby, Ionic and electronic conductivity in CaTi0. 9fe0. 1o3-δ, Ionics. 5 (1999) 385–392.

[45] L. Dunyushkina, V. Gorbunov, Crystal structure and electrical conductivity correlation in CaTi1-xFexO3-d system, Ionics. 8 (2002) 256–261.

[46] V. V. Kharton, a. P. Viskup, a. V. Kovalevsky, F.M. Figueiredo, J.R. Jurado, a. a. Yaremchenko, et al., Surface-limited ionic transport in perovskites Sr0.97(Ti,Fe,Mg)O3 − δ, J. Mater. Chem. 10 (2000) 1161–1169.

[47] R. Bredesen, J. Sogge, Paper Presented at The United Nations Economic Commission for Europe Seminar on Ecological Appli- cations of Innovative Membrane Technology in Chemical Industry, Chem/Sem. 21/R.12, Cetraro, Calabr. Italy, 1–4 May. (1996).

[48] M. Arnold, H. Wang, A. Feldhoff, Influence of CO2 on the oxygen permeation performance and the microstructure of perovskite-type (Ba0.5Sr0.5)(Co0.8Fe0.2)O3−δ membranes, J. Memb. Sci. 293 (2007) 44–52.

[49] J. Martynczuk, K. Efimov, L. Robben, A. Feldhoff, Performance of zinc-doped perovskite-type membranes at intermediate temperatures for long-term oxygen permeation and under a carbon dioxide atmosphere, J. Memb. Sci. 344 (2009) 62–70.

[50] Y. Kathiraser, Z. Wang, N.-T. Yang, S. Zahid, S. Kawi, Oxygen permeation and stability study of La0.6Sr0.4Co0.8Ga0.2O3−δ (LSCG) hollow fiber membrane with exposure to CO2, CH4 and He, J. Memb. Sci. 427 (2013) 240–249.

[51] J. Gao, L. Li, Z. Yin, J. Zhang, S. Lu, X. Tan, Poisoning effect of SO2 on the oxygen permeation behavior of La0.6Sr0.4Co0.2Fe0.8O3-δ perovskite hollow fiber membranes, J. Memb. Sci. 455 (2014) 341–348.

[52] S. Song, P. Zhang, M. Han, S.C. Singhal, Oxygen permeation and partial oxidation of methane reaction in Ba0.9Co0.7Fe0.2Nb0.1O3−δ oxygen permeation membrane, J. Memb. Sci. 415-416 (2012) 654–662.

[53] J. Yi, M. Schroeder, M. Martin, CO2-Tolerant and Cobalt-Free SrFe0.8Nb0.2O3−δ Perovskite Membrane for Oxygen Separation, Chem. Mater. 25 (2013) 815–817.

[54] K. Efimov, T. Klande, N. Juditzki, A. Feldhoff, Ca-containing CO2-tolerant perovskite materials for oxygen separation, J. Memb. Sci. 389 (2012) 205–215.

[55] M. Balaguer, J. García-Fayos, C. Solís, J.M. Serra, Fast Oxygen Separation Through SO2- and CO2-Stable Dual-Phase Membrane Based on NiFe2O4−Ce0.8Tb0.2O2-δ, Chem. Mater. 25 (2013) 4986–4993.

[56] H. Takamura, K. Okumura, Y. Koshino, a. Kamegawa, M. Okada, Oxygen Permeation Properties of Ceria-Ferrite-Based Composites, J. Electroceramics. 13 (2004) 613–618.

[57] H. Takamura, M. Ogawa, K. Suehiro, H. Takahashi, M. Okada, Fabrication and characteristics of planar-type methane reformer using ceria-based oxygen permeable membrane, Solid State Ionics. 179 (2008) 1354–1359.

[58] T. Ishihara, T. Yamada, H. Arikawa, Mixed electronic–oxide ionic conductivity and oxygen permeating property of Fe-, Co-or Ni-doped LaGaO 3 perovskite oxide, Solid State Ionics. 135 (2000) 631–636.

[59] T. Ishihara, Y. Tsuruta, T. Todaka, H. Nishiguchi, Y. Takita, Fe doped LaGaO 3 perovskite oxide as an oxygen separating membrane for CH 4 partial oxidation, 153 (2002) 709–714.

[60] H. Yamada, Viscous creep deformation of polycrystalline CaTiO3 at elevated temperatures, J. Mater. Sci. 19 (1984) 2639–2642.

[61] P. Li, S. Karato, Z. Wang, High-temperature creep in fine-grained polycrystalline CaTiO3 , an analogue material of ( Mg , Fe ) SiO 3 perovskite, 95 (1996) 19–36.

[62] J. Wolfenstine, Rate-controlling species for creep of the solid state electrolyte: doped lanthanum gallate, Solid State Ionics. 126 (1999) 293–298.

[63] I. Wærnhus, N. Sakai, H. Yokokawa, T. Grande, M.-A. Einarsrud, K. Wiik, Mass transport in La1?xSrxFeO3(x=0 and 0.1) measured by SIMS, Solid State Ionics. 175 (2004) 69–71.

[64] I. Wærnhus, N. Sakai, H. Yokokawa, T. Grande, M.-A. Einarsrud, K. Wiik, Cation diffusion in La1−xSrxFeO3−δ, x=0 and 0.1 measured by SIMS, Solid State Ionics. 178 (2007) 907–914.

[65] S. Švarcová, K. Wiik, J. Tolchard, H.J.M. Bouwmeester, T. Grande, Structural instability of cubic perovskite BaxSr1 - xCo1 - yFeyO3 - δ, Solid State Ionics. 178 (2008) 1787–1791.

[66] G. Pećanac, L. Kiesel, R. Kriegel, J. Malzbender, Comparison of thermo-mechanical characteristics of non-doped and 3 mol %, Ceram. Int. 40 (2014) 1843–1850.

[67] Y. Teraoka, H. Shimokawa, C. Kang, H. Kusaba, K. Sasaki, Fe-based perovskite-type oxides as excellent oxygen-permeable and reduction-tolerant materials, Solid State Ionics. 177 (2006) 2245–2248.

[68] Q. Li, X. Zhu, Y. He, W. Yang, Oxygen permeability and stability of BaCe0.1Co0.4Fe0.5O3−δ oxygen permeable membrane, Sep. Purif. Technol. 73 (2010) 38–43.

[69] X. Zhu, H. Wang, W. Yang, Novel cobalt-free oxygen permeable membrane., Chem. Commun. (Camb). (2004) 1130–1.

[70] A.J. Samson, M. Søgaard, P. Vang Hendriksen, (Ce,Gd)O2-δ-based dual phase membranes for oxygen separation, J. Memb. Sci. 470 (2014) 178–188.

[71] E. Tsipis, Oxygen nonstoichiometry and ionic transport in La2Ni(Fe)O4 + δ, Solid State Ionics. 179 (2008) 57–60.